

Breakdown of Conventional Winding Number Calculation in One-Dimensional Lattices with Interactions Beyond Nearest Neighbors

Amir Rajabpoor Alisepahi,¹ Siddhartha Sarkar,² Kai Sun,² and Jihong Ma^{1,3,4,*}

¹*Department of Mechanical Engineering, University of Vermont, Burlington, VT 05405, USA*

²*Department of Physics, University of Michigan, Ann Arbor, MI 48109, USA*

³*Department of Physics, University of Vermont, Burlington, VT 05405, USA*

⁴*Materials Science Program, University of Vermont, Burlington, VT 05405, USA*

Topological indices, such as winding numbers, have been conventionally used to predict the number of topologically protected edge states (TPESs) in topological insulators, a signature of the topological phenomenon called bulk-edge correspondence. In this work, we theoretically and experimentally demonstrate that the number of TPESs at the domain boundary of a Su-Schrieffer-Heeger (SSH) model can be higher than the winding number depending on the strengths of beyond-nearest-neighbors, revealing the breakdown of the winding number prediction. Hence, we resort to the Berry connection to accurately count the number of TPESs in an SSH system with a domain boundary. Moreover, the Berry connection can elucidate wavelengths of the TPESs, which is further confirmed using the Jackiw Rebbi theory. We analytically prove that each of the multiple TPES modes at the domain boundary corresponds to a bulk Dirac cone, asserting the robustness of the Berry connection method, which offers a generalized paradigm for TPES prediction.

As a special class of mechanical metamaterials (MMs) and phononic crystals (PnCs), topological MMs and PnCs endowed with anomalous wave manipulation capabilities have attracted significant attention over the past decade. Analogous to topological insulators (TIs) in quantum physics [1–4], where a topological invariant is introduced to classify different quantum states of matter. In mechanical systems, such a topological invariant can also be derived from the spectral evolution of eigenvectors, or mode shapes, from a unit cell analysis to determine the number and types of topologically protected surface/edge/corner states confining phonon modes both statically [5–10] and dynamically [11–27], usually referred to as the bulk-edge correspondence.

One illustrative example of employing a topological invariant to determine the nontrivial topologically protected edge states (TPESs) can be seen in the one-dimensional (1D) Su-Schrieffer-Heeger (SSH) model [28, 29]. Initially introduced to study solitons in polyacetylene, the SSH model was later adapted in mechanical systems to identify TPES via a winding number calculation [30–32]. As discussed in the aforementioned references and our supplemental material (SM), the two arrangements of isomers with different spring stiffness c_1 and c_2 in Fig. S1(b) represent two topologically distinct phases. When $c_1 > c_2$, the origin is excluded in the contour plot in the complex plane of the off-diagonal term in the stiffness matrix, $C(k)$, where k is the wave number in the reciprocal space, and thus, the winding number $n = 0$, signifying a trivial intra-cell-hopping phase. In contrast, when $c_1 < c_2$, the contour winds about the origin once, *i.e.*, $n = 1$, indicating a topologically non-trivial inter-cell-hopping phase, see Fig. S1(c). These gauge-dependent winding numbers can also be evaluated via the Zak phase [33] measuring the rotation of eigenvectors in the unit cell, see Fig. S2. Alternatively, the

winding number can be directly calculated from $C(k)$:

$$n = \int_{-\pi/a}^{\pi/a} \frac{1}{4\pi i} \text{tr}[\sigma_3 C'^{-1} \partial_k C'] dk, \quad (1)$$

where σ_3 is the third Pauli matrix, and C' is a chiral matrix obtained from:

$$C'(k) = C(k) - (c_1 + c_2)\sigma_0, \quad (2)$$

where σ_0 is the identity matrix. Seaming two phases with different n s creates a domain boundary where a localized mode emerges. Such an interface is topologically protected due to the intrinsic topological phase difference between the two domains.

The above discussion has been well understood and applied to systems of higher dimensions, such as the 2D quantum valley Hall effect in phononic crystals [12, 18, 32, 34–37]. Most of these studies can be simplified using mass-spring systems considering only the nearest neighbor (NN) interactions. Recently, arising attention has been devoted to mechanical metamaterials with lattice interactions beyond nearest neighbors (BNNs), achieving roton-like acoustic dispersion relations under ambient conditions similar to those observed in correlated quantum systems at low temperatures [38–43]. In addition, intriguing topological states also arise due to such BNN coupling [44, 45].

In this Letter, we report a remarkable impact of BNN couplings on bulk-edge correspondence. It is well-established that the number of TPESs is determined by the corresponding topological index, derived from the fundamental principle known as the bulk-edge correspondence. In the SSH model, the number of TPESs at a domain boundary has been believed to be governed by the difference in winding numbers between the two domains, which has been validated in systems with or with-

out BNN couplings [45]. However, in this study, by employing analytical theory, numerical simulations, and experimental investigations, we prove that the number of TPESs in the SSH model is not dictated by the winding number, but by the Jackiw-Rebbi (JR) indices associated with the JR zero modes [46].

In previously studied SSH models, the winding numbers and JR indices happened to predict the same number of TPESs. However, our investigation reveals that such a coincidence is not generic. In the presence of BNN couplings, these two indices can significantly deviate from each other, which is a key observation in our study. In such a generic setup, we prove analytically and verify numerically, that the JR indices always correctly predict the number of TPESs at a domain boundary, while the relationship between the winding number and TPESs generally fails. To further validate our theoretical prediction, we fabricate a 3D-printed 1D mechanical metamaterial model with lattice interactions inspired by Chen *et al* [38, 39] and characterize the TPESs in *torsional* vibrations using a scanning Laser Doppler Vibrometer (SLDV, Polytec PSV-500). Additionally, we show that our newly proposed topological descriptor applies to a broader range of lattices with BNN interactions beyond those presented in the main text.

To start with, we add third nearest neighbors (TNNs) with spring stiffness c' to a 1D mass-spring chain with a NN spring stiffness c and restrict the motion of identical masses to the horizontal direction, as presented in Fig. 1(a). The phonon dispersion of a pair of masses reveals that when $c' < 1/3c$, the acoustic and optical phonon bands cross at $k = \pi/a$, protected by the inversion symmetry. When $c' > 1/3c$, two additional band crossings emerge in the first Brillouin zone (BZ), as presented in Fig. 1(c). A 3D representation of the band crossing transition with c' is presented in Fig. 1(b). Derivation of the exact locations of the Dirac points due to the existence of the TNN is presented in Eqns. S7-14. The additional band folding due to strong c' s results in negative group velocities in the acoustic phonon branch, corresponding to the backward wave observed in the previous study [38]. We then break the space inversion symmetry (SIS) by applying a small perturbation to the NN spring stiffness c , *i.e.*, making $c_1 = 0.8c$ and $c_2 = 1.2c$ in the unit cell, while maintaining all the TNNs identical, which opens a band gap between acoustic and optical bands, as shown in Fig. 1(d). The winding number calculation from $C'(k)$ in Eqn. S10 for the two isomers of such a system suggests that, regardless of the strength of c' , the difference between two phases is always one, indicating one TPES at the domain boundary of the two phases. Note that, with the existence of c' , the contour plots in the complex plane are no longer circular as those shown in Fig. S1(c). With weak c' (for example, $c' = 1/10c$), they present oval shapes, as shown in Fig. 1(e), while strong c' (such as $c' = c$) creates two

additional loops along the path, Fig. 1(f). In either case, the circuit winds around the origin exactly once when $c_1 < c_2$, indicating the topological charge being $n = 1$, while excluding it when $c_1 > c_2$, thus $n = 0$, yielding a consistent n difference.

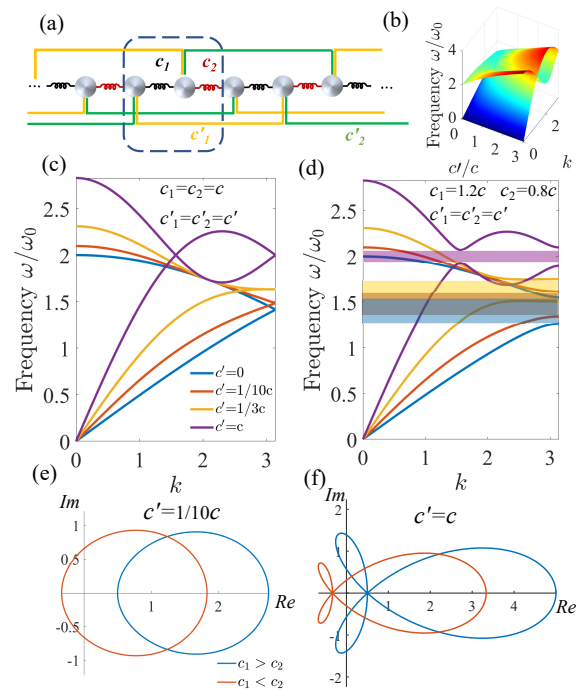


FIG. 1. (a) Unit cell (circled in a dashed line) of a chain of identical masses with nearest neighbors (NNs) with spring constants c_1 (black springs) and c_2 (red springs), and third-nearest neighbors (TNNs) with spring constants c'_1 (gold lines) and c'_2 (green lines), respectively. (b) 3D representation of phonon band variation with c' with identical NN stiffness c (with $a = 1$). (c) and (d) Unit cell band structures with various c' and (c) identical and (d) non-identical c . Shaded areas in (d) denote the bandgaps between acoustic and optical phonon branches with matching colours. (e) and (f) Contour plots of the off-diagonal element of $C'(k)$ in the complex plane for a complete circuit of k from $k = 0$ to 2π for unit cells with (e) $c' = 1/10c$ and (f) $c' = c$.

To verify the number of TPESs predicted with winding numbers, we consider a *supercell* containing 301 masses with an interface mass at the center connected to soft (stiff) springs on both sides, as shown in the left (right) schematic drawing in Fig. 2(a), about which are the symmetrically arranged two phases with different ns . Bloch conditions are applied at the two ends of the chain for phonon dispersion calculation. As predicted, when connected by weak TNNs, *i.e.*, $c' = 1/10c$, only one symmetric (asymmetric) interface mode exists within the bulk bandgap when the interface mass is connected by soft (stiff) NN springs on both sides, as shown in the supercell band structures in Fig. 2(b) with corresponding mode shapes presented in Fig. 2(c). However, when $c' = c$, we identify two additional edge modes in the bulk bandgap,

Fig. 2(e), violating the aforementioned winding number prediction. Mode shapes of these emerging bands in the bulk bandgap confirm the localization of displacements at the interface, distinguishable from the bulk modes, as shown in Fig. 2(f). When the interface mass is connected by two soft (stiff) springs $c_1 = 0.8c$ ($c_2 = 1.2c$), we obtain one (two) symmetric and two (one) asymmetric displacement fields about the interface mass. Spatial Fourier transforms (SFTs) of the mode shapes presented in Fig. 2(d) and (g) show a significantly widened peak width in all these edge modes compared to their bulk counterparts, suggesting a faster spatial decay of the vibration from the interface, evident of an edge mode. It is worth noting that, due to strong TNN interactions, the additional band crossing at $k = \pi/2$ as shown in Fig. 1(c) when $c_1 = c_2$ (which is expressed in Eqn. S14) results in the global peak (valley) of the bulk acoustic (optical) mode occurring at $k = \pi/2$, instead of $k = \pi$ where a local peak (valley) appears, as in Fig. 2(e). Hence, sharper SFT peaks appear at $k = \pi/2$ in the bulk modes closest to the bandgap (*i.e.*, SC1/2-B1/2), as shown in Fig. 2(g). Widened peaks located at $k = \pi/2, \pi$, and $3\pi/2$ are all evident in the SFTs with strong TNNs, as shown in Figs. 2(g) and S3, indicating rapid spatial decay away from the interface with hybridized wavelengths, Fig. 2(f). These interface modes at the domain boundary can also be characterized by a massless Dirac theory. For $c_1 > c_2$ ($c_1 < c_2$), the breaking of the SIS introduces a positive (negative) mass to each Dirac point. Due to the mass sign flipping at the domain boundary, one TPES in the bandgap, known as the JR zero mode, is expected to arise at the domain boundary for each Dirac cone [46]. Thus, the number of crossings presented in Fig. 1(c) within the first BZ equals the number of TPESs when the bandgap is open. The agreement of the two numbers also strongly resembles those in the quantum valley Hall effect in 2D, where the number of in-gap TPESs also matches that of bulk Dirac cones [12]. A comprehensive demonstration of the existence of one TPES corresponding to each Dirac point and their analytical solutions characterizing the spatial decay is presented in the SM. As presented in Figs. 2(d) and (g), and S3, SFTs of the analytical JR zero modes perfectly match those obtained from the supercell analysis, indicating successful predictions of the spatial decays and wavelengths of the TPESs from our JR zero mode calculations.

The question then arises as to how to determine the TPESs using a topological descriptor associating the spectral evolution of the eigenvector with these states. A closer examination of the contour plots in Fig. 1 (e) and (f) and the winding number calculation in Eqn. 1 suggests that, although the difference in n is 1 regardless of the TNN strength, trajectories of the contour plots, or the integrand of Eqn. 1, *i.e.*, the Berry connection,

$$B(k) = \frac{1}{4\pi i} \text{tr}[\sigma_3 C'^{-1} \partial_k C'], \quad (3)$$

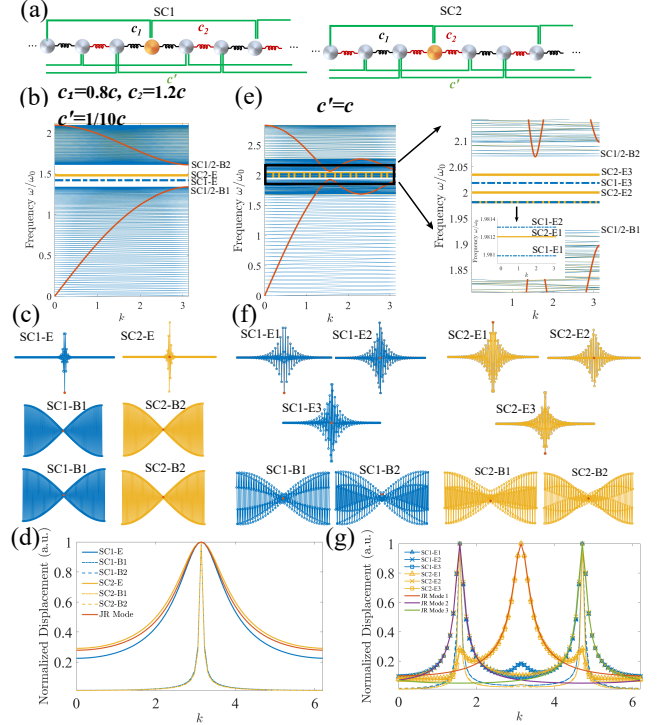


FIG. 2. (a) Supercells featuring the two arrangements of NNs with soft (stiff) springs connected to the interface mass (highlighted in orange) presented on the left (right). Both supercells contain 301 masses with Bloch conditions applied at the boundaries. (b) and (e): Band diagrams of the supercells with (b) weak ($c' = 1/10c$) and (e) strong ($c' = c$) TNNs, respectively. Blue and yellow bands correspond to soft and stiff interface springs in the left and right schematics in (a). Red curves are bulk bands acquired from the unit cell analysis in Fig. 1. Phonon bands within the bulk bandgap for the case of $c' = c$ are zoomed in next to the complete bands in (e). Dashed blue and bold solid yellow bands are edge modes, which are denoted as SC1-E(1-3) and SC2-E(1-3), respectively. Mode shapes of these edge modes for weak and strong c' are presented in (c) and (f), respectively with labels of SC1/2-E(1-3). To distinguish the edge modes from the bulk ones, bulk mode shapes for bands below and above the bandgap are also plotted in (c) and (f) with labels of SC1/2-B1/2. Red solid circles in (c) and (f) denote the displacements of interface masses. Although visualized in the vertical directions, all mass displacements are *de facto* in the horizontal direction. (d) and (g): Spatial Fourier transform (SFT) of mode shapes in (c) and (f). Solid curves are the Jackiw Rebbi (JR) zero modes derived in SM. The JR mode in (d) is plotted from Eqn. S18. JR Modes 1/2/3 correspond to Eqns. S20 and S24, respectively. The SFT plots in (g) indicate the spatial decay starting from the interface mass. The plots starting from the mass right next to the interface are presented in Fig. S3.

varies with c' , where C' is expanded to Eqn. S10 to include the TNNs. Since the number of TPESs depends on the topological invariant difference due to different gauges, we plot $\Delta B(k) = B_1(k) - B_2(k)$, where $B_1(k)$

$[B_2(k)]$ refers to the case when $c_1 < c_2$ ($c_1 > c_2$), for unit cells with different c' in Fig. 3 to describe its topology. When $c' = 0$, only one peak exists at $k = \pi$ in ΔB , corresponding to the Dirac point at $k = \pi$ in the band structure in Fig. 1(c). As c' increases while $c' < 1/3c$, this peak at $k = \pi$ decreases and widens until it splits into two smaller peaks (such as when $c' = 1/3c$). As c' continues to increase, the valley at $k = \pi$ dips below $\Delta B(k) = 0$ while the two positive peaks drift apart with locations matching Dirac points as expressed in Eqn. S14, until $k = \pi/3$ and $5\pi/3$. Meanwhile, the two peaks and one valley are further sharpened as c' increases. The integral around each peak (valley) is $+(-)1$. It is worth noting that the total integral from $k = 0$ to 2π does not change as c' varies, yielding a consistent winding number of $n = 1$. The transition from one peak in ΔB into two peaks and one valley agrees with the change of TPES counts with corresponding c' . Moreover, the locations of the peaks/valleys also match those calculated from JR zero modes in the SM and the supercell analysis, as presented in Fig. 2(d) and (g), and S3, informing of the TPES wavelengths. One can draw an analogy between the evolution of ΔB as c' decreases and the inter-valley mixing of the Berry curvature in our previously studied valley Hall effect [12]. In the current SSH model with TNNs, when $c' \gg c$, the perturbation induced by the NNs, c , is relatively small, resulting in minimal inter-valley mixing between the two peaks and one valley in ΔB , which distinctively exist in the BZ, matching the three TPESs within the bulk bandgap. As c' weakens, the difference in c becomes more prominent, introducing stronger SIS perturbation, and thus an enhanced peak-valley mixing closer to the valley at π , and eventually merging all into one single peak at $k = \pi$, leaving only one TPES in the bandgap.

It is worth noting that, compared to conventional winding number calculations, the Berry connection prediction alluded to is not limited to making correct TPES predictions in lattices with identical TNNs. As discussed in SM, one can also predict the number and the wavelengths of TPES when TNNs are nonidentical, *i.e.*, $c'_1 \neq c'_2$, as well as for systems with interactions beyond TNNs. Information about wavelengths acquired from such a Berry connection analysis is also unattainable using conventional winding number calculations. Hence, the Berry connection provides a generalized methodology supplying enriched information about TPESs in lattices with complex networks.

We proceed now to conduct experiments on 1D specimens adapted from an existing TNN model [38, 39], as shown in Fig. 4(a)-(c). Information regarding the experimental specimens is listed in SM. As presented in Fig. 4(c), each unit cell contains a pair of masses connected by alternating stiff and soft NN bars and identical TNN frames. The interface mass behind the frame labeled as E1 in Fig. 4 (e) is connected by two stiff NN

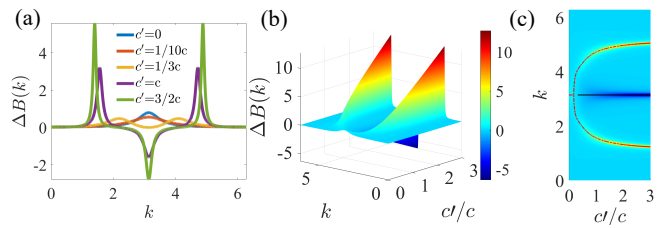


FIG. 3. (a) $\Delta B(k)$ from $k = 0$ to 2π with different c' . (b) and (c): 3D visualization of the evolution of $\Delta B(k)$ with c' . The red and black curves in the top view shown in (c) indicate peaks and valleys of the Berry connections, respectively.

connections, about which are placed with 8 unit cells with reversed stiff and soft NN arrangements. The lattice specimens are hung by a string from the top and are excited in the y -direction using an electrodynamic shaker (PCB 2007E01, powered by a Krohn-Hite 7500 amplifier) placed off-centered near the bottom left end for torsional excitation. Velocities of the left and right ends of each frame in Fig. 4(b) in the y -direction are measured by the SLDV, and their differences are recorded as the torsional velocities about the z -axis. Note that shear deformations in the y -direction will also be recorded simultaneously. However, these shear modes do not exist in our frequency range of interest. For comparison, unit cell analysis, supercell analysis containing an interface, and full-scale simulations of the lattices with the same dimensions and material parameters are also performed using COMSOL Multiphysics.

We then prescribe a chirp excitation sweeping from 800 to 1400 Hz and measure torsional velocities sampled along the axial direction of the specimen [*i.e.*, the z -axis of Fig. 4(b)]. For the specimen with strong TNNs and without an interface, we achieve an excellent agreement between the spatiotemporal spectral response obtained from a discrete Fourier transform (DFT) of the experimental data and the acoustic and optical torsional phonon branches predicted from the unit cell analysis, as shown in Fig. 4(d), presenting a roton-like dispersion relation. Frequency responses of the experimentally measured torsional velocities of the frames near the interface and in the bulk of the specimen with strong (weak) TNNs reveal three (one) distinct peaks due to amplified torsional velocities in proximity to the interface within the bulk bandgap, as evident in Fig. 4(f)[(g)]. These interface modes agree with the TPESs in supercell band structures containing matching lattice configurations with Bloch boundary conditions applied at two ends. Snapshots of the torsional velocity fields experimentally measured at bulk- and edge-mode frequencies are shown in Fig. 4(h) and (i), in which their symmetries about the interface concur with those in the toy model presented in Fig. 2(f) and (c), confirming that these interface modes are indeed TPESs predicted in theory. 3D visualization of the

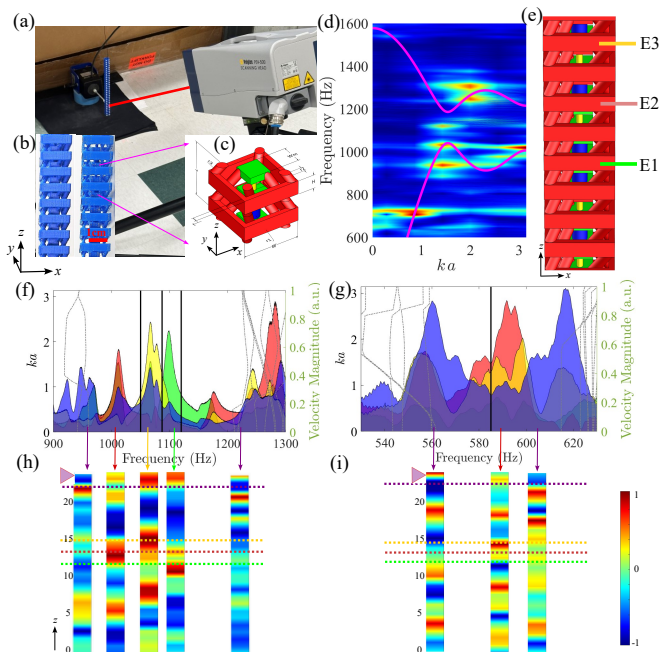


FIG. 4. (a) Experimental setup showing the SLDV head and the shaker attached near the bottom of the specimen. (b) Zoomed-in views of the specimen with strong (left) and weak (right) TNNs, with a unit cell plotted with SolidWorks in (c), in which the masses and TNN connections are represented by green blocks and red frames, respectively. The stiff and soft NN connections are shown as the blue and yellow bars between the green blocks, respectively. (d) Discrete Fourier transform (DFT) of the experimental data sampled along the specimen without the interface matching the torsional phonon bands from the unit cell analysis (magenta). (e) Zoomed-in plot around the interface mass connected by two stiff NNs (blue bars). E1, E2, and E3 indicate the frames near the interface where torsional velocities are measured and presented as green, orange, and yellow shades in (f) and (g). (f) and (g) Frequency responses (coloured shades) and band structures (dashed lines - bulk modes, solid lines - interface modes) from supercell analysis with an interface for the systems with (f) strong and (g) weak TNNs. The purple shades are acquired from a location far away from the interface. (h) and (i) Torsional velocity fields at the bulk and interface mode frequencies for the lattice with (h) strong and (i) weak TNNs. Point excitation locations are denoted with a triangle near the top end of these bars. Dashed lines with matching bar colours in (e) denote the locations of the three TNN frames. The purple dashed lines near the excitation points are measured as bulk regions.

torsional displacements from the supercell simulation is presented in Fig. S3, showing similar displacement fields as the ones obtained from experiments.

In conclusion, we have theoretically and experimentally revealed the breakdown of the conventional winding number prediction of TPESs in SSH lattices with BNN interactions. Instead, the Berry connection characterizing the evolution of eigenvectors in the reciprocal space offers more insights into the TPESs, including the num-

ber of these edge states and their wavelengths. Further, we have demonstrated that these TPESs are the phonon realization of JR zero modes, analytically validating the Berry connection prediction. Our study provides a more generalized paradigm in accurate TPES predictions in lattices beyond 1D with TNNs, which further deepens the knowledge of complex systems with multi-nodal interactions [21, 47], especially at the nano-[48] and microscales [49], where BNN interactions commonly exist, and helps with the design and characterization of phononic crystals and acousto-elastic metamaterials at large.

ACKNOWLEDGEMENT

A.R.A. and J.M. thank the University of Vermont for faculty start-up funds. S.S. and K.S. acknowledge the Office of Naval Research (MURI N00014-20-1-2479) and K.S. acknowledges the National Science Foundation (NSF Grant No. PHY-1748958) for the support of this research.

* Jihong.Ma@uvm.edu

- [1] F. D. M. Haldane, *Physical Review Letters* **61**, 2015 (1988).
- [2] C. L. Kane and E. J. Mele, *Physical review letters* **95**, 226801 (2005).
- [3] M. Z. Hasan and C. L. Kane, *Reviews of Modern Physics* **82**, 3045 (2010).
- [4] X.-L. Qi and S.-C. Zhang, *Reviews of Modern Physics* **83**, 1057 (2011).
- [5] C. Kane and T. Lubensky, *Nature Physics* **10**, 39 (2014).
- [6] J. Paulose, B. G.-g. Chen, and V. Vitelli, *Nature Physics* **11**, 153 (2015).
- [7] D. Z. Rocklin, S. Zhou, K. Sun, and X. Mao, *Nature communications* **8**, 14201 (2017).
- [8] D. Z. Rocklin, B. G.-g. Chen, M. Falk, V. Vitelli, and T. Lubensky, *Physical review letters* **116**, 135503 (2016).
- [9] O. Stenull, C. Kane, and T. Lubensky, *Physical review letters* **117**, 068001 (2016).
- [10] O. R. Bilal, R. Süssstrunk, C. Daraio, and S. D. Huber, *Advanced Materials* **29** (2017).
- [11] J. Ma, D. Zhou, K. Sun, X. Mao, and S. Gonella, *Physical review letters* **121**, 094301 (2018).
- [12] J. Ma, K. Sun, and S. Gonella, *Physical Review Applied* **12**, 044015 (2019).
- [13] R. Süssstrunk and S. D. Huber, *Science* **349**, 47 (2015).
- [14] L. M. Nash, D. Kleckner, A. Read, V. Vitelli, A. M. Turner, and W. T. Irvine, *Proceedings of the National Academy of Sciences* **112**, 14495 (2015).
- [15] P. Wang, L. Lu, and K. Bertoldi, *Physical review letters* **115**, 104302 (2015).
- [16] S. H. Mousavi, A. B. Khanikaev, and Z. Wang, *Nature communications* **6**, 8682 (2015).
- [17] T. Kariyado and Y. Hatsugai, *Scientific reports* **5**, 18107 (2015).

- [18] R. K. Pal, M. Schaeffer, and M. Ruzzene, *Journal of Applied Physics* **119**, 084305 (2016).
- [19] C. Brendel, V. Peano, O. J. Painter, and F. Marquardt, *Proceedings of the National Academy of Sciences* **114**, E3390 (2017).
- [20] R. Chaunsali, C.-W. Chen, and J. Yang, *Physical Review B* **97**, 054307 (2018).
- [21] E. Prodan, K. Dobiszewski, A. Kanwal, J. Palmieri, and C. Prodan, *Nature communications* **8**, 14587 (2017).
- [22] L. Luo, H.-X. Wang, Z.-K. Lin, B. Jiang, Y. Wu, F. Li, and J.-H. Jiang, *Nature Materials* **20**, 794 (2021).
- [23] Z. Wang and Q. Wei, *Journal of Applied Physics* **129**, 035102 (2021).
- [24] X. Ni, M. Weiner, A. Alu, and A. B. Khanikaev, *Nature materials* **18**, 113 (2019).
- [25] Y. Qi, C. Qiu, M. Xiao, H. He, M. Ke, and Z. Liu, *Physical Review Letters* **124**, 206601 (2020).
- [26] X. Zhang, H.-X. Wang, Z.-K. Lin, Y. Tian, B. Xie, M.-H. Lu, Y.-F. Chen, and J.-H. Jiang, *Nature Physics* **15**, 582 (2019).
- [27] C.-W. Chen, R. Chaunsali, J. Christensen, G. Theocharis, and J. Yang, *Communications Materials* **2**, 1 (2021).
- [28] W. Su, J. Schrieffer, and A. J. Heeger, *Physical review letters* **42**, 1698 (1979).
- [29] W.-P. Su, J. Schrieffer, and A. Heeger, *Physical Review B* **22**, 2099 (1980).
- [30] T. Lubensky, C. Kane, X. Mao, A. Souslov, and K. Sun, *Reports on Progress in Physics* **78**, 073901 (2015).
- [31] M. Esmann, F. Lamberti, A. Lemaitre, and N. Lanzillotti-Kimura, *Physical Review B* **98**, 161109 (2018).
- [32] R. K. Pal and M. Ruzzene, *New Journal of Physics* **19**, 025001 (2017).
- [33] J. Zak, *Physical review letters* **62**, 2747 (1989).
- [34] J. Lu, C. Qiu, M. Ke, and Z. Liu, *Physical review letters* **116**, 093901 (2016).
- [35] J. Lu, C. Qiu, L. Ye, X. Fan, M. Ke, F. Zhang, and Z. Liu, *Nature Physics* **13**, 369 (2017).
- [36] T.-W. Liu and F. Semperlotti, *Physical Review Applied* **9**, 014001 (2018).
- [37] T.-W. Liu and F. Semperlotti, *Physical Review Applied* **11**, 014040 (2019).
- [38] Y. Chen, M. Kadic, and M. Wegener, *Nature communications* **12**, 1 (2021).
- [39] J. A. Iglesias Martínez, M. F. Groß, Y. Chen, T. Frenzel, V. Laude, M. Kadic, and M. Wegener, *Science Advances* **7**, eabm2189 (2021).
- [40] L. Iorio, J. M. De Ponti, F. Maspero, and R. Ardito, *arXiv preprint arXiv:2211.09431* (2022).
- [41] J.-G. Cui, T. Yang, M.-Q. Niu, and L.-Q. Chen, *Journal of Applied Mechanics* **89**, 111005 (2022).
- [42] K. Wang, Y. Chen, M. Kadic, C. Wang, and M. Wegener, *Communications Materials* **3**, 1 (2022).
- [43] Z. Zhu, Z. Gao, G.-G. Liu, Y. Ge, Y. Wang, X. Xi, B. Yan, F. Chen, P. P. Shum, H.-x. Sun, *et al.*, *New Journal of Physics* **24**, 123019 (2022).
- [44] M. Grundmann, *physica status solidi (b)* **257**, 2000176 (2020).
- [45] H. Liu, X. Huang, M. Yan, J. Lu, W. Deng, and Z. Liu, *Physical Review Applied* **19**, 054028 (2023).
- [46] R. Jackiw and C. Rebbi, *Physical Review D* **13**, 3398 (1976).
- [47] K. Sun, A. Souslov, X. Mao, and T. Lubensky, *Proceedings of the National Academy of Sciences* **109**, 12369 (2012).
- [48] E. Prodan and C. Prodan, *Physical review letters* **103**, 248101 (2009).
- [49] J. Ma, *Small Science* **3**, 2200052 (2023).

Supplemental Material: Breakdown of Conventional Winding Number Calculation in Lattices with Interactions Beyond Nearest Neighbors

One-Dimensional Su-Schrieffer Heeger Model

The one-dimensional (1D) Su-Schrieffer-Heeger (SSH) model was initially introduced to understand solitons in polyacetylene, shown in Fig. S1(a), which can be simplified as a 1D chain of identical masses, m , connected by alternating springs c_1 and c_2 . The governing equations of a lattice unit cell can be expressed as

$$m\ddot{u}_1^n = c_1(u_2^n - u_1^n) - c_2(u_1^n - u_2^{n-1}), \quad (\text{S1})$$

$$m\ddot{u}_2^n = c_2(u_1^{n+1} - u_2^n) - c_1(u_2^n - u_1^n), \quad (\text{S2})$$

where displacements of the two masses in the n -th cell are denoted as u_1^n and u_2^n , respectively, and can be expressed using a plane-wave solution in combination with Bloch-Floquet periodic boundary conditions:

$$\mathbf{u}^n(t) = \tilde{\mathbf{u}}(k)e^{i(nka - \omega t)}, \quad (\text{S3})$$

where ω is the vibration frequency, \mathbf{u}^n are the displacements of the n -th cell with $\mathbf{u}^n = [u_1^n, u_2^n]$, k is the wave number, which is inversely proportional to the wavelength λ , *i.e.*, $k = 2\pi/\lambda$, a denotes the lattice constant, $\tilde{\mathbf{u}}(k)$ are displacements within the unit cell. Substituting this expression in Eqns. S1 and S2 gives:

$$[C(k) - \omega^2 m]\tilde{\mathbf{u}}(k) = 0, \quad (\text{S4})$$

where $C(k)$ is the stiffness matrix of the periodic system:

$$C(k) = \begin{bmatrix} c_1 + c_2 & -c_1 - c_2 e^{-ika} \\ -c_1 - c_2 e^{ika} & c_1 + c_2 \end{bmatrix}, \quad (\text{S5})$$

Assume $a = 1$ and divide the stiffness matrix $C(k)$ by c_2 , we can then plot the off-diagonal element of $C(k)$, *i.e.*, $\rho(k) = c_1/c_2 + e^{ika}$, and project $\rho(k)$ to a complex plane, as shown in Fig. S1(c).

The winding number difference between the two gauges can also be characterized by the Zak phase:

$$Z = \frac{i}{\pi} \int_{-\pi/a}^{\pi/a} \tilde{\mathbf{u}}_-^*(k) \partial_k \tilde{\mathbf{u}}_-(k) dk, \quad (\text{S6})$$

where $\tilde{\mathbf{u}}_-(k) = [\rho^*(k)/|\rho(k)|, 1]/\sqrt{2}$ is the eigenvector corresponding to the smaller eigenvalue of the matrix $C(k)$. Writing $\rho(k) = |\rho(k)|e^{i\phi(k)}$, we find $Z = \frac{i}{2\pi} \int_{-\pi/a}^{\pi/a} dk \partial_k (-i\phi(k)) = \frac{1}{2\pi} \int_{-\pi/a}^{\pi/a} dk \partial_k \phi(k)$. This implies that the Zak phase measures the change in the phase of the first component (in this particular choice of gauge) of the eigenvector as the wavenumber k changes from $-\pi/a$ to π/a . When $c_1 > c_2$, $Z = 0$, suggesting no changes in the phase difference of the eigenvectors across the first BZ, see the blue curve in Fig. S1(c) and Fig. S2(a). When $c_1 < c_2$, $Z = 1$, indicating a phase change of 2π within the BZ, see the red curve in Fig. S1(c) and Fig. S2(b).

One-Dimensional Su-Schrieffer Heeger Model with Third Nearest Neighboring Springs

Adding the third nearest neighbors (TNNs), as in Fig. 1(a) of the main text, modifies the governing equations to

$$m\ddot{u}_1^n = c_1(u_2^n - u_1^n) - c_2(u_1^n - u_2^{n-1}) + c'_1(u_2^{n+1} - u_1^n) - c'_2(u_1^n - u_2^{n-2}), \quad (\text{S7})$$

$$m\ddot{u}_2^n = c_2(u_1^{n+1} - u_2^n) - c_1(u_2^n - u_1^n) + c'_2(u_1^{n+2} - u_2^n) - c'_1(u_2^n - u_1^{n-1}). \quad (\text{S8})$$

Plugging the same wave ansatz in Eqn. (S3) in the above set of equations, we obtain an equation of the same form as Eqn. (S4) with the following stiffness matrix:

$$C(k) = \begin{bmatrix} c_1 + c_2 + c'_1 + c'_2 & -c_1 - c_2 e^{-ika} - c'_1 e^{ika} - c'_2 e^{-2ika} \\ -c_1 - c_2 e^{ika} - c'_1 e^{-ika} - c'_2 e^{2ika} & c_1 + c_2 + c'_1 + c'_2 \end{bmatrix}. \quad (\text{S9})$$

The chiral matrix then becomes:

$$C'(k) = C(k) - (c_1 + c_2 + c'_1 + c'_2)\sigma_0, \quad (\text{S10})$$

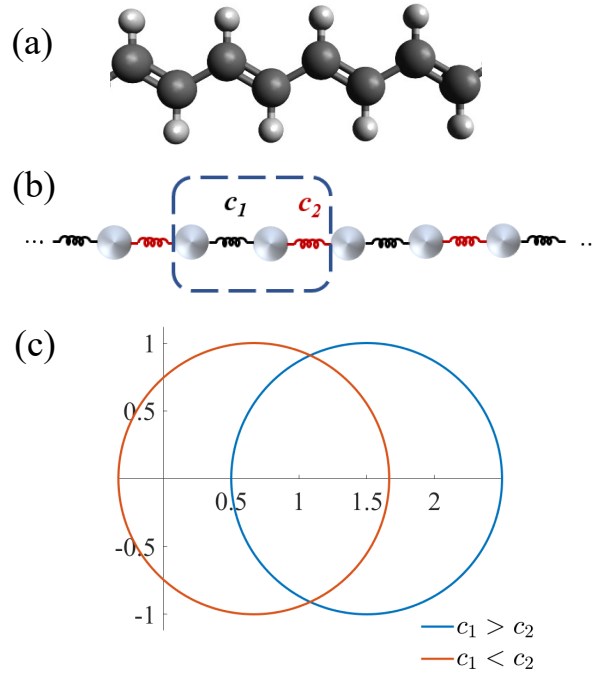


FIG. S1. (a) A polyacetylene chain created with Avogadro. (2) The simplified SSH model consists of identical masses connected by alternating spring constants c_1 and c_2 with the unit cell circled in a dashed line. (c) Contour plots in the complex plane of $\rho(k)$ for a complete circuit of k from $k = 0$ to 2π .

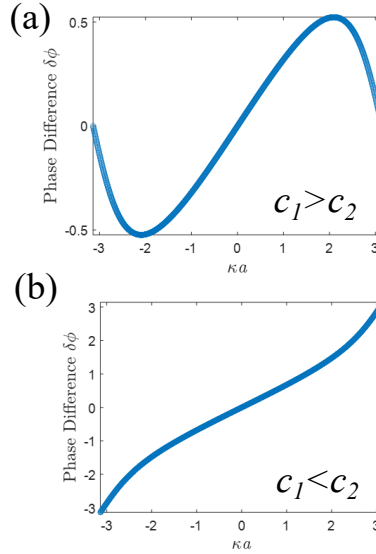


FIG. S2. Eigenvector phase difference across the first BZ for cases of (a) $c_1 > c_2$ and (b) $c_1 < c_2$.

The contour plots of the off-diagonal element of this matrix $\rho(k) = c_1 + c_2 e^{ika} + c'_1 e^{-ika} + c'_2 e^{2ika}$ for a complete circuit of k from $k = 0$ and $k = 2\pi/a$ for different values of TNN spring stiffnesses, c' , are plotted in Fig. 1(e-f) in the main text. We see that for $c_1 < c_2$ ($c_1 > c_2$) the winding number of $\rho(k)$ around the origin is 1 (0).

It is also instructive to find the values of k at which the Dirac points appear when $c_1 = c_2 = c$ and $c'_1 = c'_2 = \eta c$. To get this, we note that the band gap closes when the off-diagonal term in the matrix $C(k)$ in Eqn. S9 is zero:

$$c + \frac{c}{z} + \eta cz + \frac{\eta c}{z^2} = 0 \Rightarrow z = -1, \frac{-1 + \eta \pm \sqrt{(1 + \eta)(1 - 3\eta)}}{2\eta}, \quad (\text{S11})$$

where $z = e^{ika}$. Clearly, there are three Dirac points when $\left| \frac{-1+\eta \pm \sqrt{(1+\eta)(1-3\eta)}}{2\eta} \right| = 1$ since $z = e^{ika}$. Now, there are two cases: (i) $\frac{-1+\eta \pm \sqrt{(1+\eta)(1-3\eta)}}{2\eta}$ is real, (ii) $\frac{-1+\eta \pm \sqrt{(1+\eta)(1-3\eta)}}{2\eta}$ is complex. In the first case, we have

$$\begin{aligned} \left(-1 + \eta \pm \sqrt{(1+\eta)(1-3\eta)} \right)^2 &= 4\eta^2 \\ \Rightarrow \eta &= -1 \text{ or } \eta = 1/3 \text{ or } \eta = 0, \end{aligned} \quad (\text{S12})$$

The solution of z in Eqn. S11 prevents η from being zero since it can blow up z . A negative η is also not possible because there is no negative spring constant. Therefore, the only valid solution is $\eta = 1/3$, resulting in all three Dirac points appearing at $z = -1$, *i.e.*, $k = \pi/a$.

On the other hand, if $\frac{-1+\eta \pm \sqrt{(1+\eta)(1-3\eta)}}{2\eta}$ is complex, the requirement of the existence of three Dirac points is

$$\begin{aligned} \left(-1 + \eta + \sqrt{(1+\eta)(1-3\eta)} \right) \left(-1 + \eta - \sqrt{(1+\eta)(1-3\eta)} \right) &= 4\eta^2 \\ \Rightarrow 1 - 2\eta + \eta^2 - 1 + 2\eta + 3\eta^2 &= 4\eta^2, \end{aligned} \quad (\text{S13})$$

which is always true. Thus, if $\frac{-1+\eta \pm \sqrt{(1+\eta)(1-3\eta)}}{2\eta}$ is complex, its absolute value is always 1, regardless of the value of η . Note that this condition is only valid when $\sqrt{(1+\eta)(1-3\eta)}$ is complex, meaning $\eta > 1/3$ (since $\eta \geq 0$). Hence, combining the complex and real solutions of z , we can identify the three Dirac points for $\eta \geq 1/3$. The values of k at which these three Dirac points appear are

$$k = \frac{\pi}{a}, \pm \frac{1}{a} \arctan \left(\frac{\sqrt{(1+\eta)(3\eta-1)}}{-1+\eta} \right). \quad (\text{S14})$$

It is interesting to note that in the limit of $c' \gg c$ or $\eta \rightarrow \infty$, the three Dirac points appear at $k = \pi/a$ and $\pm\pi/3a$ (the latter of which are equivalent to $\pi/3a$, and $5\pi/3a$ from 0 to $2\pi/a$), corresponding to the band crossing locations presented in Fig. 1(c) in the main text.

The Jackiw-Rebbi Zero Modes

In this section, we demonstrate the existence of multi-interface modes at the domain boundary as shown in Fig. 2(a, e, and f) in the main text using the Jackiw Rebbi (JR) theory. With a space inversion symmetry (SIS), *i.e.*, $c_1 = c_2$, each band crossing point can be characterized by a massless Dirac theory. For $c_1 > c_2$ ($c_1 < c_2$), the breaking of the SIS introduces a positive (negative) mass to each Dirac point. Due to the mass sign flipping at the domain boundary, one topologically-protected edge state (TPES) in the bandgap, known as the JR zero mode, is expected to arise at the domain boundary for each Dirac cone[46], which explains the matching number of TPESs with $c_1 \neq c_2$ and band crossing points with $c_1 = c_2$. The agreement of the two numbers also strongly resembles those in the quantum valley Hall effect in 2D, where the number of in-gap TPESs also matches that of bulk Dirac cones [12]. Below, we provide a comprehensive demonstration of the existence of one TPES corresponding to each Dirac point and their analytical solutions characterizing the spatial decay observed in both the toy model analysis in Fig. 2 and the experimental observation in Fig. 4 in the main text.

Jackiw Rebbi Mode Corresponding to Dirac Point at $k = \pi/a$

Setting $c_1 = c + m/2$, $c_2 = c - m/2$, and $c'_1 = c'_2 = \eta c$, and expanding matrix $C'(k = \pi/a + \delta k)$ for small δk and m , we get

$$C'(\pi/a + \delta k) \approx c \begin{bmatrix} 0 & -m - i(1-3\eta)a\delta k \\ -m + i(1-3\eta)a\delta k & 0 \end{bmatrix} = -m\sigma_1 + c(1-3\eta)a\delta k\sigma_2, \quad (\text{S15})$$

where σ_i are Pauli matrices. In the above equation, m is the mass of the Dirac particle. Now, we create a domain wall at $x = 0$ with phase $c_1 > c_2$ in the region $x < 0$ and $c_1 < c_2$ in the region $x > 0$. Hence, $m(x) > 0$ for $x < 0$ and $m(x) < 0$ for $x > 0$, indicating the location dependence of mass m . Since the translation symmetry is broken due

to the presence of the domain wall, we can replace δk with $-i\partial_x$. We seek a zero frequency domain wall eigenmode $\psi(x)$:

$$\begin{aligned}
C'\psi(x) &= 0 \\
\Rightarrow (-m(x)\sigma_1 - (1-3\eta)ai\sigma_2\partial_x)\psi(x) &= 0 \\
\Rightarrow \sigma_1(-m(x)\sigma_1 - (1-3\eta)ai\sigma_2\partial_x)\psi(x) &= 0 \\
\Rightarrow (-m(x)\mathbb{1} + (1-3\eta)a\sigma_3\partial_x)\psi(x) &= 0.
\end{aligned} \tag{S16}$$

Now, there are two cases: (i) $(1-3\eta) > 0$, and (ii) $(1-3\eta) < 0$. The eigenmodes corresponding to these two scenarios are discussed below.

(i) $(1-3\eta) > 0$: Plugging the ansatz $\psi(x) = f(x) \begin{pmatrix} 1 \\ 0 \end{pmatrix}$, where $f(x)$ is a scalar function, we obtain the following differential equation for $f(x)$

$$\partial_x f(x) = \frac{m(x)}{(1-3\eta)a} \Rightarrow f(x) = c_0 e^{\frac{1}{a} \int_0^x dx' m(x') / (1-3\eta)}, \tag{S17}$$

where c_0 is a constant. Note that $f(x)$ decays exponentially away from $x = 0$, since $\frac{m(x>0)}{(1-3\eta)a} < 0$ and $\frac{m(x<0)}{(1-3\eta)a} > 0$. Recall that the zero frequency domain wall mode is at $k = \pi/a$, the full expression of the mode is

$$\psi_{\pi/a}(x) = \psi(x) e^{i\pi x/a} = c_0 e^{\frac{1}{a} \int_0^x dx' m(x') / (1-3\eta)} e^{i\pi x/a} \begin{pmatrix} 1 \\ 0 \end{pmatrix}. \tag{S18}$$

(ii) $(1-3\eta) < 0$: Plugging the ansatz $\psi(x) = f(x) \begin{pmatrix} 0 \\ 1 \end{pmatrix}$, where $f(x)$ is a scalar function, we obtain the following differential equation for $f(x)$

$$\partial_x f(x) = -\frac{m(x)}{(1-3\eta)a} \Rightarrow f(x) = c_0 e^{-\frac{1}{a} \int_0^x dx' m(x') / (1-3\eta)}. \tag{S19}$$

Similarly, $f(x)$ decays exponentially away from $x = 0$ since $\frac{m(x>0)}{(1-3\eta)a} > 0$ and $\frac{m(x<0)}{(1-3\eta)a} < 0$. The zero frequency domain wall mode being at $k = \pi/a$ leads to the full expression of the mode being

$$\psi_{\pi/a}(x) = \psi(x) e^{i\pi x/a} = c_0 e^{-\frac{1}{a} \int_0^x dx' m(x') / (1-3\eta)} e^{i\pi x/a} \begin{pmatrix} 0 \\ 1 \end{pmatrix}. \tag{S20}$$

Jackiw Rebbi Mode Corresponding to Dirac Point at $k = \pm \frac{1}{a} \arctan \left(\frac{\sqrt{(1+\eta)(3\eta-1)}}{-1+\eta} \right)$

For simplicity, we will show here the existence of zero modes for $\eta = 1$ (this is what is considered in Fig.2(e-g)), but the procedure applies to any $\eta \geq 1/3$. For $\eta = 1$, the Dirac point is at $k = \pm\pi/2a$. Away from the inversion symmetric point, when $c_1 = c + m/2$ and $c_2 = c - m/2$, expanding the matrix $C'(k = \pm\pi/2a + \delta k)$ for small δk and m :

$$\begin{aligned}
C'(\pm\pi/2a + \delta k) &\approx \begin{bmatrix} 0 & 2(\pm 1 - i)ca\delta k - m(1 \pm i)/2 \\ 2(\pm 1 + i)ca\delta k - m(1 \mp i)/2 & 0 \end{bmatrix} \\
&= -m(\sigma_1 \mp \sigma_2)/2 + 2ca\delta k(\pm\sigma_1 + \sigma_2).
\end{aligned} \tag{S21}$$

As in the case of $k = \pi/a$, we create a domain wall at $x = 0$ with phase $c_1 > c_2$ in the region $x < 0$ and the phase $c_1 < c_2$ in the region $x > 0$, implying the position-dependence of mass $m(x)$, i.e., $m(x) > 0$ when $x < 0$ and $m(x) < 0$ when $x > 0$. Since the translation symmetry is broken due to the presence of the domain wall, $\delta k \rightarrow -i\partial_x$. We seek a zero frequency domain wall eigenmode $\psi(x)$:

$$\begin{aligned}
C'\psi(x) &= 0 \\
\Rightarrow [-m(x)(\sigma_1 \mp \sigma_2)/2 - 2cai(\pm\sigma_1 + \sigma_2)\partial_x]\psi(x) &= 0 \\
\Rightarrow (\sigma_1 \mp \sigma_2)[-m(x)(\sigma_1 \mp \sigma_2)/2 - 2cai(\pm\sigma_1 + \sigma_2)\partial_x]\psi(x) &= 0 \\
\Rightarrow [-m(x)\mathbb{1} + 4ca\sigma_3\partial_x]\psi(x) &= 0.
\end{aligned} \tag{S22}$$

Plugging the ansatz $\psi(x) = f(x) \begin{pmatrix} 1 \\ 0 \end{pmatrix}$, where $f(x)$ is a scalar function, we obtain the following differential equation for $f(x)$

$$\partial_x f(x) = \frac{m(x)}{4ca} \Rightarrow f(x) = c_0 e^{\frac{1}{4ca} \int_0^x dx' m(x')}, \quad (\text{S23})$$

where c_0 is a constant. Notice that $f(x)$ decays exponentially away from $x = 0$ since $\frac{m(x>0)}{4ca} < 0$ and $\frac{m(x<0)}{4ca} > 0$. Recalling that the zero frequency domain wall mode is at $k = \pm\pi/2a$, the full expression of the mode is

$$\psi_{\pm\pi/2a}(x) = \psi(x) e^{\pm i\pi x/2a} = c_0 e^{\frac{1}{4ca} \int_0^x dx' m(x')} e^{\pm i\pi x/2a} \begin{pmatrix} 1 \\ 0 \end{pmatrix}. \quad (\text{S24})$$

The spatial Fourier transform (SFT) plots of the JR zero modes perfectly match the ones obtained from our supercell toy models presented in Fig. 2 in the main text, with Eqn. S18 plotted in Fig. 2(d), and Eqns. S20 and S24 shown in both Fig. 2(g) and Fig. S3.

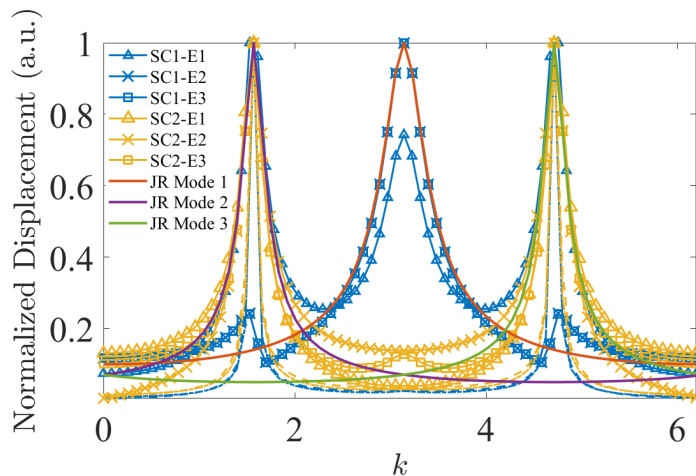


FIG. S3. Spatial Fourier transform of mode shapes in Fig. 2(f) in the main text starting from the mass right next to the interface. Solid curves are the Jackiw Rebbi zero modes discussed in SM. JR Modes 1/2/3 correspond to Eqns. S20 and S24, respectively. The SFT plots in (g) indicate the spatial decay starting from the interface mass.

Topologically Protected Edge States beyond Equal Third Nearest Neighbors

The Berry connection proposed in this work provides a generalized paradigm to predict the number of TPESs while informing of the wavelength of these edge states. The equal TNN scenario discussed in the main text is an example of when the winding number fails, but the Berry connection succeeds in predicting the number of TPESs. In cases when the effect of TNN difference dominates, the Berry connection makes the same prediction of the TPESs as the winding number does, however with additional information about the wavelength of these edge states. For example, with $c'_1 = 3c - \Delta c'$ and $c'_2 = 3c + \Delta c'$, where $\Delta c' = 0.1c$, the winding number difference between the two gauges presented in Fig. S4(d) is 1, yet $\Delta B(k)$ shows two peaks and one valley from $k = 0$ to 2π , corresponding to three distinct edge modes similar to the scenario discussed in the main text. With an enhanced c' difference, such as when $\Delta c' = 0.3c$, we obtain three distinct peaks in $\Delta B(k)$ from 0 to 2π at $k = 1.23, \pi$, and 5.05 , as presented in Fig. S4(b) and (c) which correspond to the three Dirac points predicted with Eqn. S14 with $\eta = 3$. Integration of these three local peaks all yields one, suggesting three TPESs existing in the bulk bandgap. These three TPESs also coincide with the winding number of three due to the all positive signs of the local peaks of $\Delta B(k)$. The contour plot of the off-diagonal element of $C'(k)$ (with $C'(k)$ including the TNNs expressed in Eqn. S10) also shows winding numbers of -1 and 2 for the two gauges presented in Fig. S4(e), yielding a difference of 3 between the two phases. Thus, these three TPESs can be predicted using either the Berry connection or the winding number calculation. Their existence can be confirmed by conducting a supercell analysis in the same manner described in the main text. The band diagram, mode shapes,

and the spatial Fourier transform (SFT) are presented in Fig. S4(d-f). As can be seen from the SFT plots, peak locations of the TPESs all match those in the $\Delta B(k)$ plot presented in Fig. S4(b), indicating the predictability of TPES wavelengths with Berry connections. The evolution of $\Delta B(k)$ with $\Delta c'$ also suggests the breakdown of the winding number prediction fails when $\Delta c' < 0.2c$ due to the flip of the peak and valley in $\Delta B(k)$ at $k = \pi$ due to a winding number difference of one [shown in Fig. S4(d)] as opposed to three from both the $\Delta B(k)$ calculation and the supercell analysis.

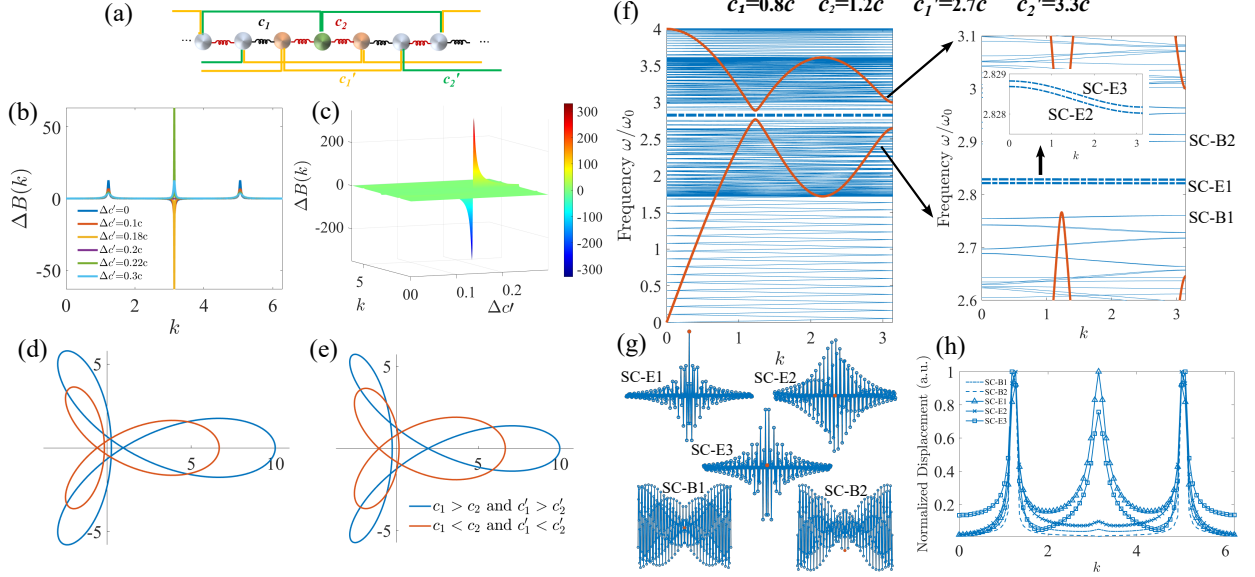


FIG. S4. (a) A supercell featuring unequal nearest neighbors with $c_1 = 0.8c$ and $c_2 = 1.2c$ with stiff springs (c_2) connected to the green interface mass, and nonidentical third nearest neighbors, $c'_1 = 3c - \Delta c'$ and $c'_2 = 3c + \Delta c'$, with strong neighbors (c'_2) connected to the green interface mass and weak (c'_1) neighbors connected to the yellow interface masses. (b) 2D and (c) 3D visualization of $\Delta B(k)$ from $k = 0$ to 2π with different $\Delta c'$. (d) and (e) Contour plots of the off-diagonal element of $C'(k)$ in the complex plane from $k = 0$ to 2π for (d) $\Delta c' = 0.1c$ and (e) $\Delta c' = 0.3c$, respectively. (f) Band diagram (blue curves) of the supercell with spring constants listed in the figure. Zoomed in are the three edge states (dashed blue curves) within the bulk bandgap (with bulk bands shown in red). Mode shapes of these edge modes are presented in (g) with labels of SC-E(1-3). To distinguish the edge modes from the bulk ones, bulk mode shapes for bands below and above the bandgap are also plotted in (g) with labels of SC-B1/2. Red solid circles in these mode-shape plots denote the displacements of the green interface mass. Although visualized in the vertical directions, all mass displacements are *de facto* in the horizontal direction. Presented in (h) is the spatial Fourier transform (SFT) of these mode shapes.

Moreover, the Berry connection calculation is also applicable to lattices beyond TNN interactions. For example, with identical TNNs (c') and fifth nearest neighbors (FNNs), c'' , and nonidentical nearest neighbors, the winding number difference is still one, as shown in Fig. S5(a). However, the Berry connection $\Delta B(k)$ reveals three peaks and two valleys, Fig. S5(b), suggesting five TPESs existing in the bulk bandgap. Indeed, from the supercell analysis with a similar setup as shown in Fig. 2(a) and S4(a), five edge modes emerge within the bulk bandgap, Fig. S5(c), with their mode shapes presented in Fig. S5(d). SFT of these five TPESs reveals that all these TPES modes are a hybridization of five wavelengths with wave numbers corresponding to the locations of the peaks and valleys shown in Fig. S5(b). One can prove in a similar fashion that as long as the differences in the beyond nearest neighbors are sufficiently small, the winding numbers of two gauges will always yield zero and one, which fails in predicting the actual number of TPESs that can be conveniently captured by the $\Delta B(k)$ calculation.

Experimental Specimen Information

The specimens are 3D-printed (Stratasys F170 FDM 3D Printer) using acrylonitrile butadiene styrene (ABS) with the following parameters: Young's modulus $E=1.5$ GPa, Poisson's ratio $\mu=0.35$, and density $\rho=1250$ kg/m³. As presented in Fig. 4(c), each unit cell contains a pair of masses (green cubes) with side length $W_m=6$ mm, connected by 5 mm-nearest-neighboring (NN) struts with alternating radii, $r_1=3.52$ mm (blue) and $r_2=1.47$ mm (yellow), to

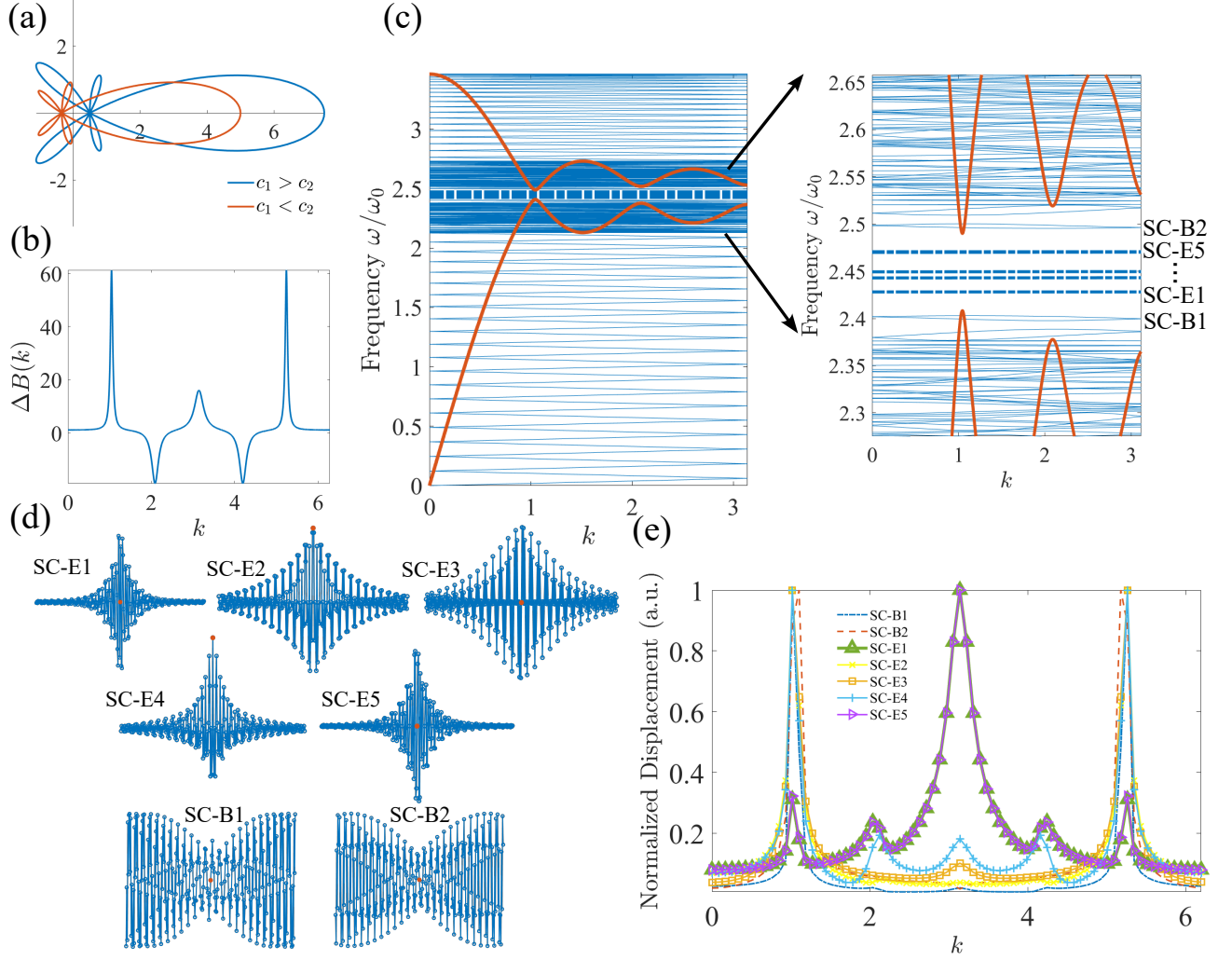


FIG. S5. (a) Contour plots of the off-diagonal element of $C'(k)$ in the complex plane and (b) $\Delta B(k)$ from $k = 0$ to 2π for a lattice with identical third ($c' = c$) and fifth ($c'' = c$) nearest neighbors and nonidentical nearest neighbors $c_1 = 1.2c$ and $c_2 = 0.8c$. (c) Band diagram (blue curves) of the supercell with spring constants listed in the figure. Zoomed in are the three edge states (dashed blue curves) within the bulk bandgap (with bulk bands shown in red). Mode shapes of these edge and bulk modes are presented in (d) with labels of SC-E(1-3) and SC-B1/2, respectively. Red solid circles in these mode-shape plots denote the displacements of the interface mass. Although visualized in the vertical directions, all mass displacements are *de facto* in the horizontal direction. Presented in (e) is the spatial Fourier transform (SFT) of these mode shapes.

enable stiffer and softer NN interactions, respectively. Strong (weak) TNNs are established by a combination of red squared frames with side length $W=16$ mm, height $H=4$ mm (3.2 mm), and thickness $t=1.33$ mm (1.07 mm), and bars with radius $r_3=2.43$ mm (1.28 mm) connecting the masses and frames. Mode shapes of the three (one) edge modes and two bulk modes with strong (weak) TNNs modeled by COMSOL Multiphysics with these material properties and structural dimensions are presented in Fig. S6.

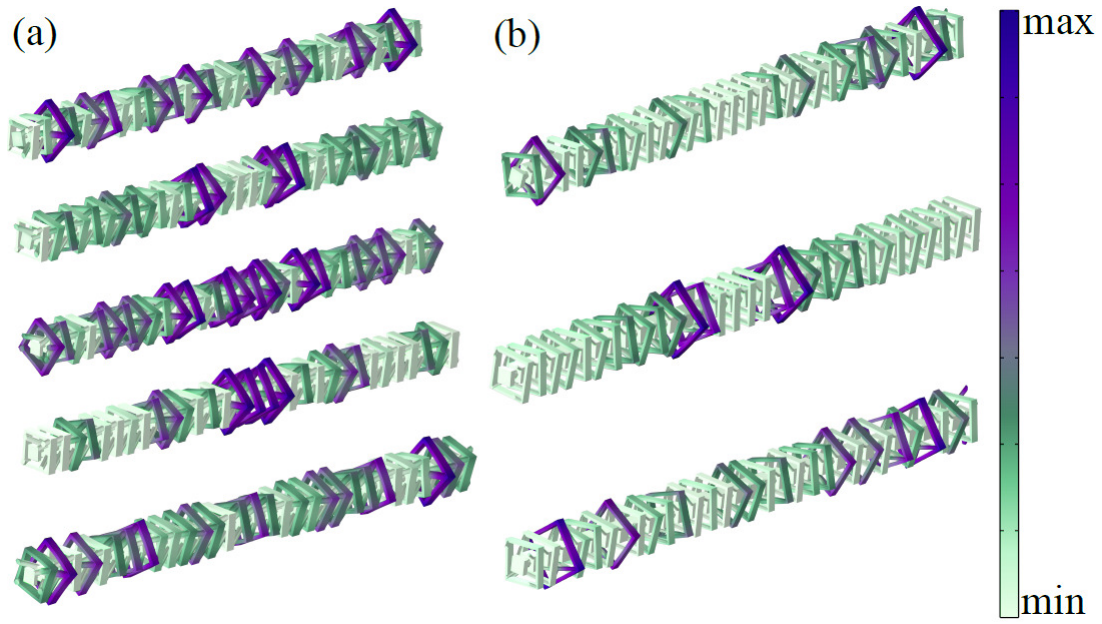


FIG. S6. 3D visualization of the torsional displacements from the supercell analysis of the lattice with (a) strong and (b) weak third nearest neighbors. The top and bottom mode shapes in each column are the two bulk modes. The ones in between are the edge states. Symmetries and locations of the deformed frames all match well with the ones obtained from experiments presented in Fig. 4(h) and (i). The colour bar shows the magnitude of the displacements.